SECONDARY ATOMISATION: SIMULATION OF DROPLET BREAK-UP IN DISTURBED FLOW FIELDS

F. Bierbrauer, T.N. Phillips

School of Mathematics, Cardiff University, Cardiff, CF24 4AG, UK

Abstract

It is well known that both combustion efficiency in diesel engines, and the the quenching of fires, is conditioned by the surface to volume ratio of fuel/water droplets. This requires a deeper understanding of the droplet break-up process within liquid sprays. The break-up of individual droplets follows well known behaviour although how nearby droplets in the spray influence this process is not well understood. By numerically simulating the break-up behaviour of two equally sized droplets in two distinct geometrical configurations it is shown that the break up of each droplet is strongly influenced by the presence of the other.

INTRODUCTION

Fuel injection plays an important role in combustion and emissions performance of diesel engines [6]. Liquid fuel is sprayed into the combustion chamber through spray nozzles with induced cavitation leading to fuel jet breakup or primary atomisation. It is well known that combustion efficiency in diesel engines, gas turbines and oil burners is conditioned by the delay of fuel evaporation which is directly influenced by the droplet size distribution [10, 2]. The smaller the diameter of individual droplets the shorter the evaporation time, thereby improving fuel-air mixing and combustion [2]. After primary atomisation the liquid patches, sheets or ligaments, which are inherently unstable, lead to secondary break-up [13] of individual droplets. There are two main break-up mechanisms: (i) aerodynamic break-up where the relative velocity between the droplet and the continuous gaseous phase is sufficient to fragment the droplet and (ii) collision induced break-up where colliding droplets may coalesce and, given sufficient energy, cause further disruption of the droplets [6]. The first of these processes is controlled by the Weber number which, depending on the relative velocity between the droplet and the gas, induces so-called bag, stripping or catastrophic break-up [13]. On the other hand collision induced break-up is classified into four different kinds: bounce, coalescence, reflexive separation and stretching separation which depend on the Weber number, droplet size ratio and an impact parameter. The last two, reflexive and stretching separation, can give rise to satellite droplets which further reduce initial droplet sizes [8].

The previously mentioned aspects of secondary atomisation are well known and have been investigated for the break-up of individual droplets in a high speed gas flow [13] as well as the collision of a pair of droplets [8]. However, the global flow is a combination of dispersed liquid within an ambient gas and other droplets within its vicinity, especially in the case of dense sprays [14]. In addition, during spray droplet break-up and transport the gas phase gains significant momentum from the droplets leading to gas-phase turbulence [13]. Further turbulent droplet break-up may then occur through collisions between turbulent eddies and a droplet [1]. Break-up occurs when the distorting hydrodynamic stress associated with a turbulent eddy exceeds the restoring stress of droplet surface tension [7]. This is equivalent to saying that individual droplets are immersed within a disturbed flow field.

Previous research has been oriented towards investigating the overall process of secondary atomisation through phenomenological models taking into account the Rayleigh-Taylor and Kelvin-Helmholtz break-up mechanisms, making use of numerous empirical correlations, and through reduced fluid dynamical models such as TAB [9,10]. Turbulent eddy induced break-up, on the other hand, has been dealt with separately [14, 1, 7]. Some modelling work has been done on droplet break-up by numerically solving the Navier-Stokes (NS) equations to obtain the local behaviour of the flow for individual droplets [3, 16]. In each case the phenomena have been studied individually.

It is the aim of this paper to simulate droplet break-up when an individual droplet is influenced by others in its vicinity. This may involve how the ambient gas stream is shielded by surrounding droplets before impacting on the droplet of interest as well as the influence of inter-droplet gaseous turbulent eddies induced by the dispersed flow. As a first stage in the numerical modelling of the droplet break-up process, this paper will concentrate on the solution of the unsteady, viscous, incompressible, two-phase Navier-Stokes equations in two dimensions. This paper uses an Eulerian-Lagrangian method, the Godunov Marker-Particle Projection Scheme, to implicitly track fluid interfaces in a Lagrangian manner and update fluid variables on an Eulerian grid [3]. This involves how droplets shelter other droplets from the bulk flow as well as altering how this flow impacts other droplets.
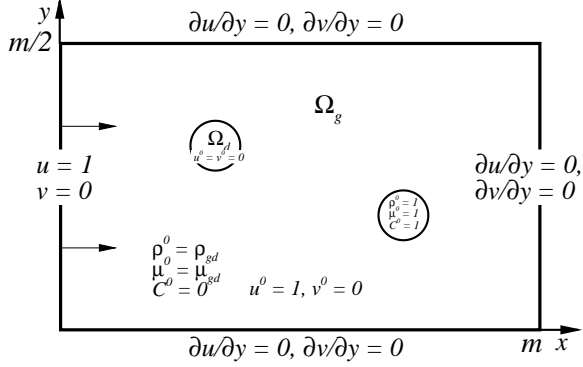
Figure 1: Configuration of the droplet break-up problem.

GOVERNING EQUATIONS

We consider a one-field formulation of the governing equations for unsteady incompressible flow. The non-dimensionalised Navier-Stokes equations are solved in the domain $\Omega = \{(x,y) : 0 < x,y < m\}$ with $\Omega = \Omega_a \cup \Omega_d$ where Ω_a represents the region of the domain occupied by an ambient fluid and Ω_d that of the droplet fluid. Thus, for two-phase flow, the governing equations written in dimensionless form are

$$\frac{\partial \mathbf{u}}{\partial t} + (\mathbf{u} \cdot \nabla)\mathbf{u} = -\frac{1}{\rho}\nabla p + \frac{1}{\rho Re}\nabla \cdot \mu \mathbf{D} + \frac{\kappa(\mathbf{x})\nabla\rho}{We[\rho]\langle\rho\rangle},$$
$$\nabla \cdot \mathbf{u} = 0,$$
$$\frac{\partial C}{\partial t} + \mathbf{u} \cdot \nabla C = 0$$
$$\rho = C + (1-C)\rho_{ad},$$
$$\mu = (C + (1-C)/\mu_{ad})^{-1} \tag{1}$$

where $\mathbf{D} = \nabla\mathbf{u} + \nabla\mathbf{u}^T$ and we have non-dimensionalised with respect to: length-initial droplet diameter D_d, velocity-initial droplet impact velocity U_d, density-droplet density ρ_d, viscosity-droplet viscosity μ_d, pressure-$\rho_d U_d^2$ and time-the convective time D_d/U_d scale. The Reynolds and Weber numbers are defined by $Re = \rho_d U_i D_d/\mu_d$ and $We = \rho_d U_i^2 D_d/\sigma_{gd}$. The density and viscosity ratios are: $\rho_{gd} = \rho_g/\rho_d$, $\mu_{gd} = \mu_g/\mu_d$. The volume fraction $C = C_d$ so that $C_a = 1 - C_d$. The surface force term is expressed through the curvature $\kappa(\mathbf{x}) = \nabla\cdot\mathbf{n}$ where $\mathbf{n} = \nabla\rho/|\nabla\rho|$ is the normal to the interface, the jump in density across the interface is $[\rho] = 1 - \rho_{gd}$ and average of the densities is given by $\langle\rho\rangle = (1 + \rho_{gd})/2$. Dimensional domain lengths are L taken as an integer multiple of droplet diameter, $m = L/D_d$.

Boundary conditions are (i) a known inflow at the left boundary, $\mathbf{u}(0,y,t) = (1,0)$ and (ii) truncated outflow conditions along the left, top and right boundaries $\partial\mathbf{u}/\partial n = \mathbf{0}$. No flux conditions on the density, viscosity and consequently the volume fraction are used for all

boundaries, i.e. $\mathbf{n}\cdot\nabla\rho|_{\partial\Omega} = \mathbf{n}\cdot\nabla\mu|_{\partial\Omega} = \mathbf{n}\cdot\nabla C|_{\partial\Omega} = 0$. Although no pressure boundary conditions are required, projection methods make use of a gauge variable ϕ to ensure satisfaction of an approximate solenoidal velocity field. Gauge variable boundary conditions are homogeneous Neumann conditions (i) $\mathbf{n} \cdot \nabla\phi|_{\partial\Omega} = 0$ except along (ii) outflow boundaries where Zhu [17] recommends $\partial\phi/\partial\tau|_{\partial\Omega} = 0$. This last condition may be integrated along the outflow part of the boundary to yield $\phi|_{\partial\Omega} = $ constant. The condition $\phi|_{\partial\Omega} = 0$ at outflow is sometimes implemented in the literature. Initial densities and viscosities were constant in each fluid and all initial pressures were zero. Initially, we prescribe $\mathbf{u}^0 = \mathbf{i}$ in the ambient fluid and $\mathbf{u}^0 = \mathbf{0}$ in the droplet.

THE NUMERICAL METHOD

The semi-implicit projection method

The system (1) is solved using the approximate Godunov projection method [11] with second-order Crank-Nicolson time discretisation. Given the strengths and weaknesses of the various projection methods we choose to use a modified version of the incremental pressure projection method of Rider *et al.* [12]. The original method uses a time-lagged discretization of the pressure gradient in the momentum equation, sets the intermediate velocity boundary conditions to the physical boundary conditions and uses a homogeneous Neumann condition in the projection stage of the algorithm. The modification to this method uses a corrected pressure update to ensure consistency and incorporates a variable density.

In semi-discrete form, this results in the following pressure corrected, variable density, second-order approximation of the equations in (1) at time t^n:

1. Step 1: Given $\mathbf{u}^n$, $\nabla p^{n-1/2}$, ρ^n, μ^n, C^n calculate $(\mathbf{u} \cdot \nabla\mathbf{u})^{n+1/2}$

2. Step 2: update C^{n+1} so that

$$\rho^{n+1} = C^{n+1} + (1-C^{n+1})\rho_{ad},$$
$$\mu^{n+1} = \left(C^{n+1} + (1-C^{n+1})/\mu_{ad}\right)^{-1} \tag{2}$$

and define $\rho^{n+1/2} = (\rho^n + \rho^{n+1})/2$ and $\mu^{n+1/2} = (\mu^n + \mu^{n+1})/2$.

3. Step 3: solve for the intermediate velocity

$$\left(\mathbf{I} - \frac{\Delta t}{2Re}\sigma^{n+1/2}L_\mu^{n+1/2}\right)\mathbf{u}^* = \left(\mathbf{I} + \frac{\Delta t}{2Re}\sigma^{n+1/2}L_\mu^{n+1/2}\right)\mathbf{u}^n$$
$$-\Delta t\left((\mathbf{u}\cdot\nabla\mathbf{u})^{n+1/2} + \sigma^{n+1/2}\nabla p^{n-1/2} - \sigma^{n+1/2}\mathbf{F}^{n+1/2}\right) \tag{3}$$

4. Step 4: project the result

$$L_\sigma^{n+1/2}\phi^{n+1} = \frac{1}{\Delta t}\nabla \cdot \mathbf{u}^* \tag{4}$$

followed by

$$\mathbf{u}^{n+1} = \mathbf{u}^* - \Delta t \sigma^{n+1/2} \nabla \phi^{n+1} \qquad (5)$$

5. Step 5: update the pressure gradient

$$\begin{aligned} \nabla p^{n+1/2} &= \nabla p^{n-1/2} + \nabla \phi^{n+1} - \\ &\quad \frac{\Delta t}{2Re} L_\mu^{n+1/2} \left(\sigma^{n+1/2} \nabla \phi^{n+1} \right) \end{aligned} \qquad (6)$$

where $\mathbf{F} = \kappa(\mathbf{x})\rho \nabla \rho / (We[\rho]\langle\rho\rangle)$ and the Laplacian operators are given by $L_\mu \mathbf{w} = \nabla \cdot \mu (\nabla \mathbf{w} + (\nabla \mathbf{w})^T)$, for a vector $\mathbf{w}$, and $L_\sigma \psi = \nabla \cdot \sigma \nabla \psi$, for a scalar ψ, $\sigma = 1/\rho$, $\sigma^{n+1/2} = (\sigma^n + \sigma^{n+1})/2$ and $\bar{\Omega} = \Omega \cup \partial\Omega$. The $(\mathbf{u} \cdot \nabla \mathbf{u})^{n+1/2}$ term represents an approximation to the nonlinear advection term at the half time level and is the one detailed in [11]. The velocity at the half time level has also been used in the viscous term and is given by $\mathbf{u}^{n+1/2} = (\mathbf{u}^n + \mathbf{u}^*)/2$. The extra pressure correction term $-(\Delta t/2Re)L_\mu \sigma \nabla \phi$ was obtained by eliminating the intermediate velocity in the momentum equation (3) using the update given by (5).

Note that in the projection method described above the time updated density and viscosity is required in Step 1 where only the values at the nth time level are known. This is calculated with the use of the Godunov Marker-Particle Projection Scheme (GMPPS) [4] where fluid particles are advanced forward in time to track individual fluid phases while carrying particle colour information. The time updated volume fraction for the fluid phase C^{n+1} is then obtained by interpolation from surrounding fluid particles of that phase. This provides the solution of the advection equation for the volume fraction.

The smoothing of discontinuities

Since there are discontinuities in the physical properties, such as density and viscosity, an element of smoothing is necessary. In practice, the volume fraction is smoothed by forming the convolution of C with a kernel $K(\mathbf{x}; \epsilon)$ which becomes the surface delta function as $\epsilon \to 0$ [5]. That is

$$\tilde{C}(\mathbf{x}) = \int_{\Omega_K} C(\mathbf{x}')\mathbf{K}(r; \varepsilon) \, d\mathbf{x}' \qquad (7)$$

where $r = |\mathbf{x}' - \mathbf{x}|$. Here, Ω_K is the compact support of the kernel, or the points for which $\mathbf{K}(r; \varepsilon) \neq 0$ and ε the the size of the support. Ideally, a kernel should possess compact support, be monotonically decreasing with respect to r, be radially symmetric, be sufficiently smooth, be a good representation of the delta function as $|\Omega_K| \to 0$ and possess the normalisation property $\int_{\Omega_K} \mathbf{K}(r; \varepsilon) \, d\mathbf{x} = 1$ [15]. In the present case we choose the eighth degree polynomial kernel because it closely matches all of the properties listed above, being superior to say the Nordmark kernel which is not monotonically decreasing and tends to produce highly singular

oscillations as $|\Omega_K| \to 0$ [15]. The kernel is defined by

$$\mathbf{K}_8(r; \varepsilon) = \begin{cases} \frac{5}{\pi \varepsilon^2}[1 - (r/\varepsilon)^2]^4 & \text{if } r < \varepsilon \\ 0 & \text{otherwise} \end{cases}$$

At any point (x, y) in the domain the volume fraction there may be convolved by considering a circle of radius ε, $(x' - x)^2 + (y' - y)^2 = \varepsilon^2$, the support of the kernel, and integrating (7). The evaluation of this integral requires a little care when examining points near the boundary, within one cell width, as the support of the kernel may overlap the boundary therefore requiring ghost cells as part of the evaluation. A finite number of ghost cells indicates that the smoothing length shouldn't exceed two to three cell widths.

Spatial discretisation of differential operators

We use a collocated grid defined in [4] for the velocity and pressure $\mathbf{u}_{i,j}$, $p_{i,j}$ for $i = 1, 2, 3, ..., I$, $j = 1, 2, 3, ..., J$ with cell edges used to define the boundaries at $x_{1/2}, y_{1/2} = 0$, $x_{I+1/2}, y_{J+1/2} = m$. Discrete differential operators are second order accurate cell-centred discretisation as detailed in [5]. The discretised convective term in the NS equations is detailed in [11]. Boundary conditions are imposed along the left, right, top and bottom most cell edges and determine ghost cell values required by the discretisation. Time step restrictions include a CFL condition as well as terms involving the various forces acting

$$\Delta t < \frac{1}{2} \min_{\substack{1 \le i \le I \\ 1 \le j \le J}} \left(\frac{\Delta x}{|u_{i,j}^n|}, \frac{\Delta y}{|v_{i,j}^n|}, \frac{3Re}{14} \frac{\rho_{i,j}^n(\Delta x^2, \Delta y^2)}{\mu_{i,j}^n}, \right.$$

$$\left. \sqrt{\frac{2(\Delta x, \Delta y)}{F_{i,j}^n}} \right) \qquad (8)$$

where

$$F_{i,j}^n = \left| -\sigma_{i,j}^n (\mathbf{G}p)_{i,j}^{n-1/2} + \frac{\sigma_{i,j}^n}{Re}(L_\mu \mathbf{u})_{i,j}^n \right.$$

$$\left. + \frac{\kappa_{i,j}^{n+1/2}(\mathbf{G}\rho)_{i,j}^{n+1/2}}{We[\rho]\langle\rho\rangle} \right|$$

Filtering of velocity data

One of the drawbacks associated with approximate projection methods on collocated grids is the existence and growth of null spaces in the discrete divergence operator giving rise to 'checkerboard modes' where the discrete operator fails to recognise non-divergence-free modes [12]. This is manifested as high frequency noise in the discrete divergence of the velocity. Through the use of iterated projection filters, which diffuse divergent modes, and velocity filters, which subtract off unphysical modes from the velocity field, these spurious modes are mostly removed [12]. Filters are best used

in conjunction at the end of a computational cycle and are essential for two-phase flows with large density ratios which, if not applied, create spurious velocity fields resulting in noise, asymmetry and eventually instability [12, 9]. Both projection and velocity filters are used in this paper.

NUMERICAL RESULTS

The current investigation will concentrate on how the droplet break-up process is altered due to the influence of neighbouring droplets. We follow the experimental study of Theofanus *et al* [14] investigating the break-up of droplets under the influence of uniform inflow for (i) a single droplet, (ii) two droplets of equal size located a distance, $L_x/D_d = 2$, one directly behind the other, and (iii) two droplets of equal size diagonally separated with distances $L_x/D_d = 2$, $L_y/D_d = 1$, see Figure 2. These cases are designated Series A, B and C. In all cases considered $D_d = 0.0049$m, $\rho_d = 1000$

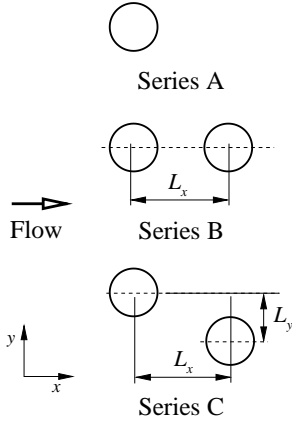Figure 2: Geometric configurations considered for one and two, free-to-move, droplets of equal size

kg/m^3, $\mu_d = 0.001$ kg/ms and $\sigma_{gd} = 0.072$ N/m. The calculations take place inside a domain of size $10D_d \times 5D_d$ with a 256×128 grid. To determine the break-up conditions the Weber number is varied through the inflow velocity U_i. Note that we also refer to the gas Weber number $We_G = \rho_g U_i^2 D_d/\sigma_{gd}$ commonly used to analyse the break-up process [3, 14]. The characteristic deformation time scale is often taken to be at a time of $T = D_d/U_i\sqrt{\rho_d/\rho_g}$ [14]. In the following set of graphical results the impact plots show the $C = 1/2$ contour which best matches the interface position. All individual figures are read left to right, top to bottom. The total simulation time was $t = 5$ non-dimensional time units with a total of 20 time steps saved over this range. Each plot is taken at the 0, 5, 10, 15 and 20th saved time step.

$\underline{We_G = 7}$

In this case we consider the break-up of either one or two droplets for an inflow velocity of $U_i = 10$ m/s giving a gas Weber number of $We_G = 7$.

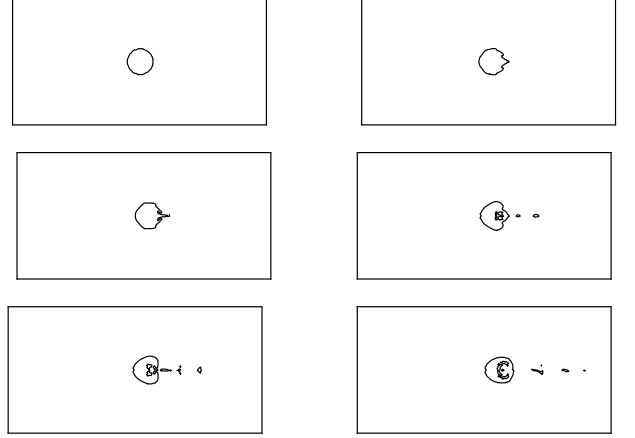Figure 3: The Series A case with $We_G = 7$, $Re_G = 4900$.

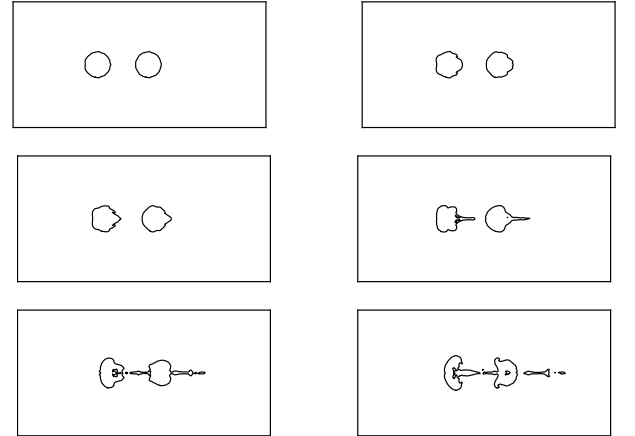Figure 4: The Series B case with $We_G = 7$, $Re_G = 4900$.

$\underline{We_G = 62}$

In this case we consider the break-up of either one or two droplets for an inflow velocity of $U_i = 16$ m/s giving a gas Weber number of $We_G = 62$.

DISCUSSION AND CONCLUSIONS

We discuss the results by first comparing the behaviour of Series A,B and C scenarios for the $We_G = 7$ case followed by the $We_G = 62$ case.
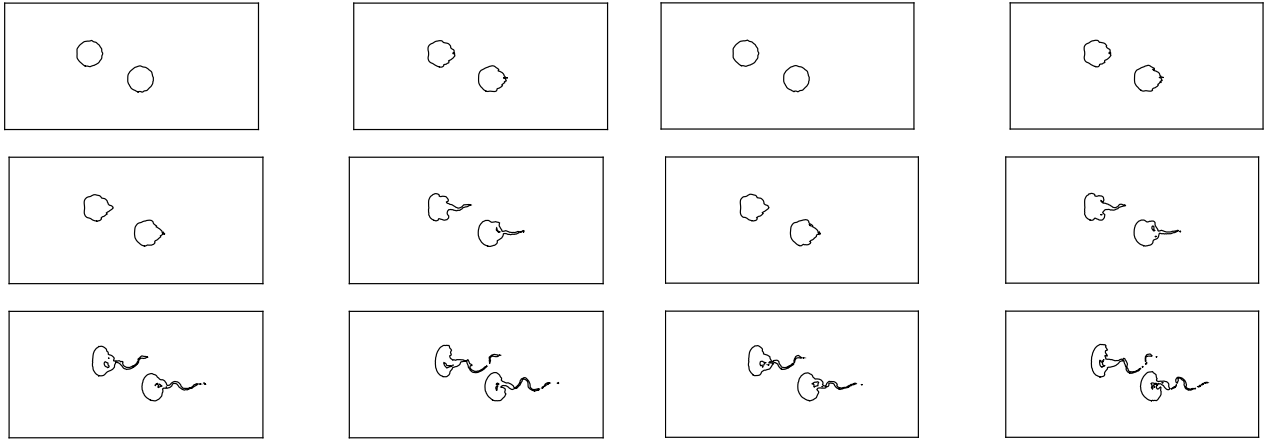
1. $\underline{We_G = 7}$

Figure 5: The Series B case with $We_G = 7$, $Re_G = 4900$.

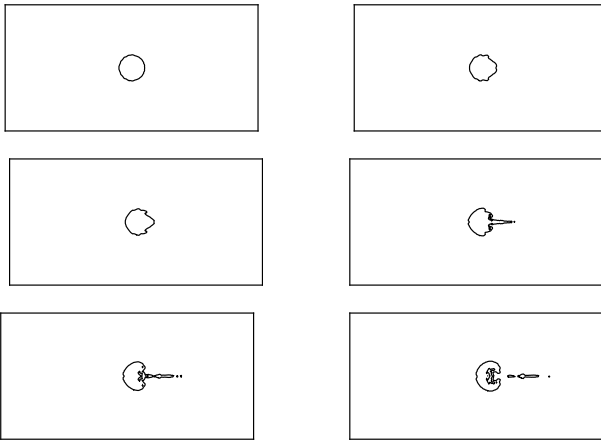Figure 8: The Series B case with $We_G = 62$, $Re_G = 14700$.

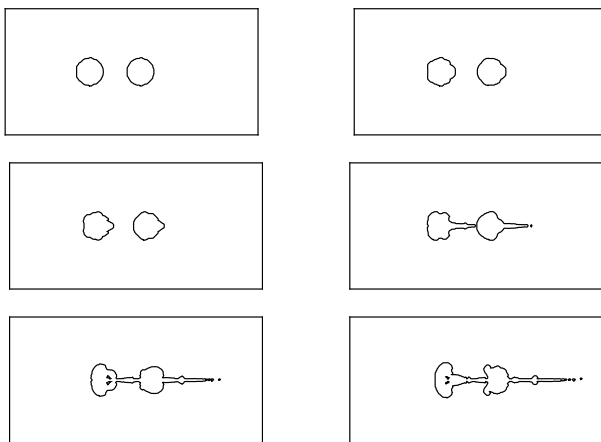Figure 6: The Series A case with $We_G = 62$, $Re_G = 14700$.

Figure 7: The Series B case with $We_G = 62$, $Re_G = 14700$.

(a) *single droplet break-up*: it is clear from Figure 3 that, while the boundary conditions confine the droplet within the top and bottom boundaries to some degree, it is nonetheless free to break up in the lengthwise direction. The break-up progresses by first forming a pinched off section along the symmetry line behind the droplet which gradually elongates and breaks up further downstream. Two small vortices form along the symmetry line just inside the droplet giving rise to a concavity on the droplet surface. This concavity grows until it starts to penetrate the droplet while aiding the expulsion of droplet material at its rear.

(b) *comparison of single and shielded break-up*: In this scenario, series B in Figure 4, the droplet further downstream is sheltered by the droplet on its upstream side. While the start of the droplet break-up process is similar to that of the single droplet case it is clear that the actual vortex development, noticed in series A, occurs at a later stage. The upstream droplet now behaves very differently from that of the series A case in that it starts to stretch in the downstream direction. The following plot indicates that the upstream droplet now starts to enter the vortex development stage and also starts to eject a fluid filament which impacts on the downstream droplet. The last plot shows that this fluid filament acts to deform the downstream droplet although it does not seem to cause actual disruption.

(c) *comparison of shielded and diagonal break-up*: in series C, Figure 5, the initial droplet deformation behaviour is quite similar to series A and B although by the fourth plot in the series the flow around the upstream droplet starts to disturb the break-up of the upstream droplet. Both expel an oscilla-

tory fluid filament in the downstream direction. Both droplets now also lose symmetry in their break-up characteristics one on the side above the symmetry line and the other on the opposite side. The vortex development seen earlier which causes a concavity is now hindered and proceeds more slowly especially in the downstream droplet when compared to that in Figure 4. In the final plot most of the individual droplet mass is lost through the expulsion of the oscillatory stream instead of vortex development.

2. <u>$We_G = 62$</u>

(a) *single droplet break-up*: a comparison of Figures 3 and 6 shows a difference in break-up behaviour already by the second of the plots. It appears that the $We = 62$ case forms a bulge on its downstream side rather than a pinch off as seen in the $We = 7$ case. Again, as the simulation proceeds vortex development takes place at an earlier stage than for the $We = 62$ case. The downstream filament is expelled earlier although is not of the same size as the latter. Finally the formation of a concavity within the downstream side of the droplet progresses more deeply in the $We = 62$ case.

(b) *comparison of single and shielded break-up*: the break-up characteristics of Figures 4 and 7 show a great deal of similarity for the first few plots. By the fourth plot the $We = 62$ case starts to form long fluid filaments about one and half times as long as the $We = 7$ case. These filaments also appear to be more substantial. Considerably more fluid is ejected in the latter case and the stream ejected from the upstream droplet appears to penetrate the downstream one and pass through it. Vortex development is also enhanced in both droplets.

(c) *comparison of shielded and diagonal break-up*: the plots of Figures 5 and 8 on the other hand both appear to be very much the same in character, other than a small difference in internal vortex structure. Note that while the donwstream filaments thrown off by each droplet appear oscillatory no vortices are shedded by either droplet. This is not unexpected for the subsonic droplet break-up case [14].

From the simulations it is clear that the droplet break-up process is significantly different for each droplet in series B and C than for that of series A. While the downstream droplet in series B case is sheltered by the upstream droplet it is also severely deformed by the downstream filament ejected from the upstream droplet. In the case of series C each droplet is affected by the other so that its break-up behaviour is markedly changed from either that of series A or B. The downstream filaments formed are now of an oscillatory character although no vortices are shedded by the droplet. While this characteristic filament-vortex structure development is much the same for both the $We = 7$ and $We = 62$ cases, the latter produces stronger downstream filaments.

ACKNOWLEDGEMENT

NOMENCLATURE

Symbol	Quantity	SI Unit
u	Velocity	m/s
p	Pressure	kg/ms^2
ρ	Density	kg/m^3
μ	Viscosity	Ns/m^2
C	Volume fraction	dimensionless
σ	Surface tension	N/m

References

[1] R. Andersson and B. Andersson. Modeling the breakup of fluid particles in turbulent flows. *AIChE J.*, 52:2031–2038, 2006.

[2] P. Berthoumieu, H. Carentz, P. Villedieu, and G. Lavergne. Contribution to droplet breakup analysis. *Int. J. Heat Fluid Flow*, 20:492–498, 1999.

[3] F. Bierbrauer and T.N. Phillips. The numerical prediction of droplet deformation and breakup using the Godunov marker-particle projection scheme. *Int. J. Numer. Methods Fluids*, 56:1155–1160, 2008.

[4] F. Bierbrauer and S.-P. Zhu. A numerical model for multiphase flow based on the GMPPS formulation, part I: kinematics. *Comput. Fluids*, 36:1199–1212, 2007.

[5] F. Bierbrauer and S.-P. Zhu. A numerical model for multiphase flow based on the GMPPS formulation, part II: dynamics. *Eng. Appl. Comput. Fluid Mech.*, 2:284–298, 2008.

[6] T. Bo, D. Clerides, A.D. Gosman, and P. Theodossopoulos. Multidimensional modelling of diesel combustion and emissions formation. Proc 1st Meet. Greek Section Combust. Inst., Athens, Greece, November 28-29 2007.

[7] V. Cristini, J. Blawzdziewicz, M. Loewenberg, and L.R. Collins. Breakup in stochastic Stokes flows: Sub-Komolgorov drops in isotropic turbulence. *J. Fluid Mech.*, 492:231–250, 2003.

[8] G.-H. Ko and H.-S. Ryou. Modeling of droplet collision-induced breakup processes. *Int. J. Multiphase Flow*, 31:723–738, 2005.

[9] D.B. Kothe. *Free Surface Flows*, pages 267–331. Springer, New York, 1999.

[10] Z. Liu and R.D. Reitz. An analysis of the distortion and breakup mechanisms of high speed liquid drops. *Int. J. Multiphase Flow*, 23:631–650, 1997.

[11] E.G. Puckett, A. Almgren, J.B. Bell, D.L. Marcus, and W.J. Rider. A high-order projection method for tracking fluid interfaces in variable density incompressible flows. *J. Comput. Phys*, 130:269–282, 1997.

[12] W.J. Rider, D.B. Kothe, S.J. Mosso, J.H. Cerutti, and J.I. Hochstein. Accurate solution algorithms for incompressible multiphase flows. 33rd Aerospace Sciences Meeting, Reno, NV, US, November 28-29 1995.

[13] H. Shi and C. Kleinstreuer. Simulation and analysis of high-speed droplet spray dynamics. *J. Fluids Eng.*, 129:621–633, 2007.

[14] T.G. Theofanus, G.J. Li, T.N. Dinh, and C.-H. Chang. Aerobreakup in disturbed subsonic and supersonic flow flelds. *J. Fluid Mech.*, 593:131–170, 2007.

[15] M.W. Williams, D.B. Kothe, and E.G. Puckett. Convergence and accuracy of kernel-based continuum surface tension models. Proc 13th US Natl Congress of Appl Mech, Gainesville, Florida, USA, June 16-21 1998.

[16] S. Zaleski, J. Li, and S. Succi. Two-dimensional Navier-Stokes simulation of deformation and breakup of liquid patches. *Phys. Rev. Lett.*, 75:244–247, 1995.

[17] J. Zhu. The second-order projection method for the backward-facing step flow. *J. Comput. Phys.*, 117:318–331, 1995.